Magnetohydrodynamic effects in a shock-accelerated gas cylinder

Wolfgang J. Black,[1] Roy C. Allen,[1] W. Curtis Maxon,[1]
Nicholas Denissen,[2] and Jacob A. McFarland[1,*]
[1]*Mechanical and Aerospace Engineering, University of Missouri, E2412 Lafferre Hall, Columbia, Missouri 65211, USA*
[2]*Los Alamos National Laboratory, Los Alamos, New Mexico, USA*

(Received 6 July 2018; published 1 April 2019)

This work presents two-dimensional (2D) simulations on a cylindrical Richtmyer-Meshkov instability (RMI) in magnetohydrodynamics (MHD). Three studies are presented in an effort to quantify and qualify the evolution of the MHD RMI by varying the magnetic field orientation, strength of the magnetic field, and strength of the shock wave driving the instability. The orientations considered herein are either parallel or perpendicular to the shock wave motion. The second study varies the magnetic fields between 100, 250, and 500 gauss (G), while the third study considers incident shock wave Mach numbers $M = 1.2$, $M = 1.66$, and $M = 2.2$. These parameter ranges were selected to be easily achievable in experiments while the interface perturbation was selected such that its evolution is independent of either the shock wave or magnetic field orientations independently. It was found that the MHD RMI evolution is dependent upon the magnetic field orientation relative to the shock transit direction as well as their individual magnitudes. This is because the mechanism of suppression, attributed to Alfven waves, is a function of the magnetic field strength and the orientation of the magnetic field, while the mechanism of RMI evolution, baroclinic vorticity deposition, is a function of the Mach number. Stronger magnetic fields were found to provide greater mixing suppression and have significant effects on RMI-like interface morphology. Finally, increasing the shock wave strength generated competing effects between higher RMI vorticity deposition and greater vorticity removal from the interface by faster Alfven waves.

DOI: 10.1103/PhysRevFluids.4.043901

I. INTRODUCTION

As high-energy-density (HED) research continues to grow, magnetohydrodynamics (MHD) has become an important research field because of its presence in various applications. In astrophysics, where the physical medium is typically ionized and can experience magnetic fields, the inclusion MHD effects can provide physicists with greater insight into cosmological evolution [1,2]. Engineered HED systems, like inertial confinement fusion (ICF) studied at the National Ignition Facility (NIF), typically experience an array of complex physical phenomena from shock-driven accelerations to solid-plasma phase change. The transition to a plasma state alone encourages the consideration of MHD effects, but some systems may be further complicated by externally applied magnetic fields. For example, experiments performed at the Laboratory for Laser Energetics utilizing the Omega Laser on NIF capsules incorporated an external magnetic field [3], thus exhibiting MHD interactions between the plasma and the magnetic field. A promising potential alternative to ICF is magnetized liner inertial fusion (MagLIF), where a target undergoes

*mcfarlandja@missouri.edu

magnetically driven compression and then is laser heated to extreme temperatures while being magnetically confined [4,5]. Similar to the NIF and OMEGA experiments, MagLIF also experiences shock-driven hydrodynamics, phase change to plasma, and an external magnetic field; thus, understanding how magnetohydrodynamics affect these instabilities can provide much needed insight into improving the experimental yield of these processes [6–8].

In much of the research directed toward HED systems, however, a classic hydrodynamics approach is often taken. While this can provide important insight, once the system transitions into a plasma state, the necessary physics required to accurately understand the system transition from hydrodynamics into the study of electrically conducting fluids. This is even more important in the presence of an external magnetic field, where MHD effects can cause significant departure from classic hydrodynamics [9]. One area of research which has provided significant insight into the hydrodynamics of these systems is the study of the Richtmyer-Meshkov instability (RMI). The study of the RMI has been applied in astrophysics, where its inclusion increases accuracy when modeling the behavior of super novae [10]. It has been observed in ICF where shock waves penetrate several layers of different densities with perturbations in each layer. These layers experience both the RMI and the Rayleigh-Taylor instability (RTI) [9,11]. Because of the instabilities at these layers, the local electron temperatures are lowered and the energy yield potential is rapidly diminished; therefore, it is desirable to mitigate the growth of these instabilities.

The RMI [12,13] is a hydrodynamic instability resulting from three main ingredients: a pressure gradient, a density gradient, and some misalignment between them. The pressure gradient, provided by a shock wave (impulsive acceleration), propagates through the misaligned density gradient and deposits vorticity. The dependence upon the interaction of these ingredients can be seen in the baroclinic term in the vorticity conservation equation, Eq. (1). The vorticity, ω, is a function of u, ν, ρ, and P, or the velocity, kinematic viscosity, density, and pressure, while the subscripts t, i, j, and k denote time and spatial coordinates. This vorticity then acts to stretch the area of the interface, or the density gradient, and rapidly increases the mixing, driving a stable interface to eventually transition toward decaying turbulent mixing:

$$\frac{\partial \vec{\omega}}{\partial t} + (\vec{u} \cdot \nabla)\vec{\omega} = (\vec{\omega} \cdot \nabla)\vec{u} - \vec{\omega}(\nabla \cdot \vec{u}) + \left[\frac{1}{\rho^2}\nabla\rho \times \nabla P\right]_{\text{baroclinic}}. \tag{1}$$

The amount of vorticity deposition is directly related to the strength of the pressure and density gradients. The strength of the pressure gradient can be represented by the Mach number, $M = u_1/a$, with a larger M depositing more vorticity. M is a function of the fluid velocity over the speed of sound in that fluid, a. The density gradient is given by the Atwood number, $A = (\rho_2 - \rho_1)/(\rho_2 + \rho_1)$, a nondimensional ratio of the differences between ρ_2 and ρ_1 to their sum; here the subscripts 1 and 2 differentiate the upstream and downstream (interface) fluids respectively. Just as M and A represent the strength of the pressure and density gradients, the misalignment of the two can be considered as the linearity of the interface, η_0/λ, or the amplitude of the interface over the wavelength. It was shown by Richtmyer's [12] linear model that the lower this ratio is, the weaker the instability that will form, and vice versa.

While experiments have been done which may include the MHD RMI, these experiments were done in large-scale facilities (e.g., MagLIF [4,5] and OMEGA [3] experiments) and were not done to study this particular instability. However, the literature which explores the RMI can still provide insight for these applications. To better understand the RMI, experimentalists have studied various interface perturbations, species for the density gradient, and methods to create pressure gradients. While the most common way to create the pressure gradient experimentally is in a mechanical shock tube, which utilizes the release of high pressure into a lower pressure region, both laser-driven shock waves [14] and gravity-driven sleds [15,16] have been utilized. Experimentalists have also studied a wide range of interface configurations. Gas-bubble interactions have been used to deposit a bubble of ρ_2 into a shock tube containing a gas at ρ_1 [17]. Similarly, other groups have flown gas cylinders into a shock tube to create the density gradient [18–20]. Spherical and cylindrical

interfaces both create a two-interface system as the shock wave must travel from one density, into the sphere or cylinder, and back out into the original fluid, and thus share similar theory. The work presented within this paper will consider a cylindrical interface in a shock tube environment through simulations. More traditional wavelike interfaces have been studied as well, where some groups have generated a sinusoidal interface [21–23] or used the shear-flow Kelvin-Helmholtz instability [24]. A half-wavelength-like inclined interface was also studied extensively experimentally and in simulations [25–28].

While the authors know of no MHD RMI experiments done to date, there have been groups who have begun to study the MHD RMI through simulations and theory. Samtaney [29] studied an inclined MHD RMI, with a magnetic field parallel to the shock wave direction, and compared it to an inclined RMI without a magnetic field. In this work, it was shown that the magnetic field suppresses RMI growth and mixing. Wheatley *et al.* [30–32] and Mostert *et al.* [33,34] continued this work and studied a sinusoidal interface in planar and converging cylindrical and spherical geometries. Across several articles, these authors performed a full parametric study to include the effects of magnetic field orientation, increasing M, the ratio of η to λ, Atwood number, and nondimensional magnetic strength. The nondimensional magnetic strength, shown in Eq. (2), represents the ratio of thermodynamic pressure to magnetic pressure and is a function of the magnetic permeability, μ_0, and the magnetic field strength, B. They found that while the Mach number and Atwood number effects were similar to those in classic hydrodynamics, by varying the orientation of the magnetic field to be normal or transverse to the interface, the RMI in MHD would exhibit different qualitative evolution and suppressed growth rates, and that increasing the magnetic field strength further dampened the instability.

Although the MHD RMI is a relatively new field, there is a wealth of literature which explores the RMI through simulations which can be informative. While this research focuses on the RMI without MHD effects, these methods and codes are often used to inform researchers on fusion applications and astrophysics [35,36]. Many of these codes solve the hydrodynamics through nominally second-order large-eddy simulations utilizing Eulerian [37–39] and arbitrary Lagrangian-Eulerian schemes [27,40] for a wide range of perturbations and initial conditions. Other have used higher order methods [41–43]. This work will utilize the second-order arbitrary Lagrangian-Eulerian hydrocode FLAG, developed at Los Alamos National Laboratory, which is discussed further in Sec. II and in previous works [44,45]:

$$\beta = \frac{2P\mu_0}{B^2}. \tag{2}$$

To better illustrate the differences between the RMI and the MHD RMI, Fig. 1 shows a simple schematic of their evolutions through time. Figure 1(a) shows the traditional RMI with a cylindrical interface. Here a pressure gradient, shown as a shock wave, travels through a shock tube domain and eventually transits the interface. This interface provides the density gradient and is either another species with a different density or the same species at a different thermodynamic state. During the interaction of these two misaligned gradients, baroclinic vorticity is deposited along the interface. Typically, the shock wave then travels past the interface and down the domain while the interface moves at the postshock velocity and eventually transitions to turbulent mixing due to the vorticity deposition. However, this is not always the case in MHD.

It was previously mentioned that when compared to the RMI, the MHD RMI can show significant suppression of mixing [29–31]. This suppression can be attributed to waves, which exist in MHD but not in classic hydrodynamics, that work to remove vorticity from the interface. These waves are known to be both hydromagnetic and magnetosonic waves [32], the effects of which can be seen in Fig. 1(b). In this figure, waves form at the interface due to the presence of the magnetic field. As vorticity is deposited along the interface, a velocity gradient appears with components both perpendicular and parallel to the interface. These disturbances, or velocity components, are then propagated away from the interface due to the magnetic field as either Alfven waves, for the velocity along the magnetic field, or magnetosonic waves, for the velocity perpendicular to the magnetic field [46].

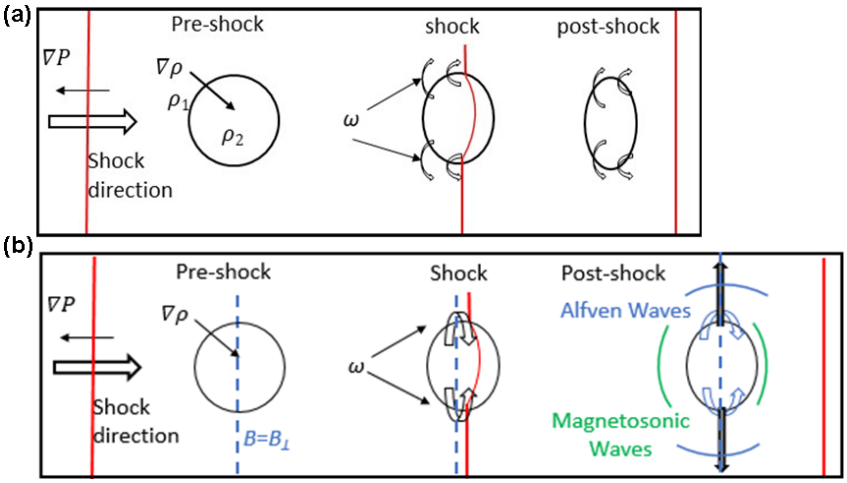

FIG. 1. Two-dimensional (2D) schematic of the cylindrical Richtmyer-Meshkov instability driven by a shock wave in (a) traditional hydrodynamics and (b) with magnetohydrodynamic effects.

Thus, in the presence of a sufficiently strong magnetic field, the RMI in MHD is suppressed as the mechanism of growth is no longer able to act on the interface. Figure 1(b) shows a magnetic field orientation perpendicular to the shock transit. For any field orientation, both magnetosonic and Alfven waves will occur, acting to stretch and remove the vorticity from the interface, though the degree of and mechanisms for damping the RMI change with orientation of the field to the shock direction.

Similarly, one can find the dispersion relation for these waves when considering the ideal MHD equations. The transition from classic hydrodynamics to MHD demands additions to the equations used to solve these systems. These ideal MHD equations are shown as Eqs. (3) through (8) and are the continuity, momentum, energy, Ampère's law, and Gausss law of magnetism, respectively. While the continuity equation, Eq. (3), remains unchanged and is only a function of the density and velocity, the other equations are either modified or complete additions to the system of equations.

The momentum equation, Eq. (4), has the addition of the electromagnetic forces which are represented by the cross product of the current density, shown as J, and the magnetic field, given as $\epsilon_{ijk}J_jB_k$ over the speed of light, c. This term is the Lorentz force without an externally applied electric field. Ampère's law expands the Lorentz force in as Eq. (6) to give Eq. (7). This form of the Lorentz force has a right-hand side whose first term gives the magnetic tension force that acts to straighten any disturbed magnetic field lines giving rise to the MHD waves and the magnetic pressure. Equation (5) contains e, which is the total energy per unit volume.

It is the interaction of the motion of charge, either parallel or perpendicular to the magnetic field, that gives rise to the MHD waves. In fact, the MHD wave dispersion equations can be easily derived for either orientation [46]. While the derivation will not be covered within this work, the dispersion relations are used to find the velocity at which the MHD waves propagate. A MHD wave will propagate perpendicular to a magnetic field at the Alfvén velocity, given as $v_A = B/\sqrt{\mu_0\rho}$. This wave is known as the hydromagnetic wave and is a function of the magnetic field strength. Similarly, the MHD wave which propagates along a magnetic field line is called the magnetosonic wave, which can be calculated as Eq. (9). The velocity of this wave is in terms of the phase velocity, Ω/k. This wave is sometimes called a fast hydromagnetic wave as it can be written as a function of the Alfvén velocity, v_A. The magnetosonic velocity is also a function of the speed of light and the acoustic velocity or c, and v_s. Its important to note that the magnetosonic velocity will tend toward the acoustic velocity as B goes to 0. It is the hydromagnetic waves which suppress the RMI in MHD by removing the vorticity from the interface. This is because the vortical motion acts to disturb the

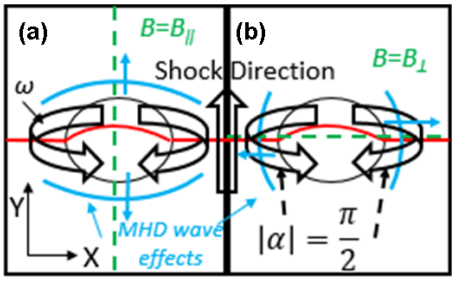

FIG. 2. A 2D schematic representing the effects of the magnetic field orientation relative to the shock wave direction on vorticity. (a) The magnetic field is perpendicular to the shock wave direction cause vortex translation normal to the shock wave. (b) The magnetic field is now parallel to the shock wave, causing vortex translation parallel to the shock wave. In both magnetic field orientations, the site of maximum baroclinic vorticity deposition is $|\alpha| = pi/2$.

magnetic field and the magnetic tension force which arises, Eq. (7), acts to restore the field at the Alfvén velocity.

$$\frac{\partial \rho}{\partial t} - \nabla(\rho \vec{u}) = 0, \tag{3}$$

$$\rho\left(\frac{\partial}{\partial t} + \vec{u} \cdot \nabla\right)\vec{u} = \frac{1}{c}\vec{J} \times \vec{B} - \nabla, P \tag{4}$$

$$\frac{\partial e}{\partial t} + \nabla \cdot \left[\left(e + P + \frac{B^2}{2}\right)\vec{u} - \vec{B} \cdot \vec{u}\,\vec{B}\right] = 0, \tag{5}$$

$$\vec{J} = \frac{c}{4\pi}\nabla \times \vec{B}, \tag{6}$$

$$\vec{J} \times \vec{B} = \frac{(\vec{B} \cdot \nabla)\vec{B}}{\mu_0} - \nabla\frac{B^2}{2\mu_0}, \tag{7}$$

$$\nabla \cdot \vec{B} = 0, \tag{8}$$

$$\frac{\Omega}{k} = \sqrt{c^2\frac{v_s^2 + v_A^2}{c^2 + v_A^2}}. \tag{9}$$

In consideration of the research done in the literature previously and with future experiments in mind, this work will explore a cylindrical interface of perfectly conducting gases in the presence of a magnetic field through simulations. The simulations presented are 2D in Cartesian coordinates and consider a 2D (R-Θ) slice of a cylinder interface with a planar shock wave. The nomenclature of cylindrical will be adopted with consideration for previous RMI literature on both experiments and simulations. The simulation conditions were selected to be achievable in experiments at the University of Missouri Fluid Mixing Shock Tube Laboratory (FMSTL) [47]; additionally, the cylindrical interface was chosen for its unique geometry. The nature of the cylinder is such that it provides a double interface [18–20] and does not have a preferential direction with respect to the shock wave or the magnetic field. However, the growth of the cylindrical interface exhibits a dependence on the orientation of the magnetic field relative to the shock wave. In Fig. 2, the shock wave is shown traveling in the Y direction. This means the site of maximum vorticity deposition is $|\alpha| = \pi/2$. However, if the shock wave direction was changed such that it was traveling in X, the maximum vorticity would occur on $|\alpha| = 0$, or orthogonal to the shock wave direction. Assuming the interface is allowed to evolve uninterrupted by boundaries and magnetic fields, the evolution of the cylindrical RMI would be the same between these two cases.

However, in the presence of a magnetic field, the evolution becomes suppressed and MHD waves work to carry the vorticity away in the direction of the magnetic field. If both the shock wave and magnetic fields are aligned, the Alfvén waves work to transport the vorticity away in the direction of the flow (shock transit direction). This is shown in Fig. 2(a), with the vorticity being stretched in Y, the direction of the shock wave motion. Similarly, Fig. 2(b) presents a scenario where the shock wave is traveling in Y and the magnetic field is in X, or perpendicular to the shock wave direction. Here, the vorticity is carried perpendicularly away from and through the interface. Thus, for other perturbations, such as the classically studied sine wave, one may be interested in transverse or normal field orientation relative to the interface; for the cylindrical interface, it does not make sense to discuss normal and transverse directions to the interface but rather the orientation of the shock wave (pressure field) to the magnetic field. In this way, the cylindrical interface is unique as it is independent of the direction of the shock wave and is only sensitive to the orientation of the fields relative to each other. While work has been done on a converging cylindrical and spherical interface, both the density and pressure gradients shared the radial geometry [33,34]. Therefore, to study the cylindrical perturbation in the MHD RMI, this paper will present simulations which will explore the orientation of the magnetic field with respect to the shock wave, the strength of the magnetic field, and the shock wave Mach number effects.

II. COMPUTATIONAL ENVIRONMENT

A. FLAG code description

The 2D simulations presented in this work were performed using the hydrocode FLAG [48,49]. FLAG is a multimaterial, multiphysics hydrodynamics code developed at Los Alamos National Laboratory (LANL). FLAG includes a fully unstructured grid mesh, allowing an arbitrary polyhedral mesh, and can function as an arbitrary Lagrangian-Eulerian (ALE) code utilizing a Lagrangian hydrodynamics step followed by an optional relaxation and remapping step [50,51]. The relaxation algorithm in the current work is a Laplacian-type smoothing and is performed every cycle. The FLAG remapping step uses the flux corrected transport (FCT) algorithm of Boris and Book [50,52] to achieve second-order accuracy for smooth solutions, while preserving monotonicity at discontinuities and ensuring conservation. The implementation is directionally unsplit in 2D/3D, based on Zalesak's work [53], and limited gradients are computed with the unstructured Barth-Jespersen limiter [54]. Experience suggests both FCT and gradient limiting are necessary for high-strain-rate flows on highly deformed meshes. Multimaterial interfaces are reconstructed using Youngs' volume of fluid method (VOF) [55]. FLAG utilizes the ideal MHD equations, shown above as Eqs. (3) through (8) and utilizes a Poisson solver for divergence control. In addition to treating the materials as perfect conductors, FLAG also solves the γ law equation of state, shown in Eq. (10). Here, γ is the ratio of specific heats and e is the internal energy for the fluid. While FLAG has resistivity capabilities, the current work does not consider two-fluid MHD, resistivity, or Hall effects:

$$P = \rho(\gamma - 1)e. \tag{10}$$

B. Simulation parameters and initial conditions

The simulation parameters for all cases are given in Table I. All simulations consider a cylindrical interface with a diameter of 2 cm. This interface is perfectly conducting nitrogen gas at 2500 K. The interface bulk temperature was selected in regards to the process of ionizing nitrogen at atmospheric conditions. The interface is surrounded by air at 300 K, and the unshocked region is initialized at standard atmospheric pressure. Figure 3, an annotated pseudocolor of plasma mass fraction (species 2 per the Atwood number definition) given as Υ_P, shows the initial conditions common to all simulations. Here, the shock wave is represented by a planar black line and with an arrow showing the direction of motion. A diffuse interface was chosen to due to the large temperature difference between the interface and its surroundings. This figure also has a thin line visible in the diffusion

TABLE I. Initial conditions.

	B	$B_\parallel$	$B_\perp$
B (G)	0	100, 250, 500	100, 250, 500
β		2550, 410, 100	2550, 410, 100
P_0 (Pa)		101,325	
T_1 (K)		300	
T_2 (K)		2500	
ρ_{air} (kgm^{-3})		1.12	
ρ_{N_2} (kgm^{-3})		0.136	
A	0.79		
M	1.2	1.66	2.2
U_{ps} (ms^{-1})$\pm$ 1%	108	311	514
D_i (cm)		2	

layer which represents the 5% plasma species contour line and is visible in all images for clarity. While this figure shows the interface, it does not show the boundaries in either the X or Y directions. This slice shows the interface at time $t = 0$ and is a 5-cm by 5-cm area centered around the interface, this scheme will be used repeatedly throughout this work. The full domain is 20 cm by 2000 cm with reflecting boundaries in X and Y respectively. The resolution in all simulations is 100 nodes per centimeter (200 nodes per cylinder diameter) and all images are visualized using the computational postprocessing software ENSIGHT, developed by Computational Engineering International, Inc.

To investigate the effects of the magnetic field on the MHD RMI, simulations were conducted over a wide range of parameters. The parameter ranges were selected with the design of future experiments in mind. The first parameter considered is the magnetic field orientation where the traditional RMI, $B = 0$ is compared to cases with a perpendicular, $B = B_\perp$, or parallel magnetic field, $B = B_\parallel$, of 500 Gauss (G). These cases all share $M = 1.66$, a Mach number realizable within our shock tube [47], and $A = 0.79$. This study is presented in Sec. III A. After the orientation effects are presented, the magnetic field strengths for both orientations are varied as 100, 250, and 500 G. This range of field strengths was selected for two reasons: First, this range is easily achievable for experimentalists even when considering a shock tube domain, and second, if observable suppression

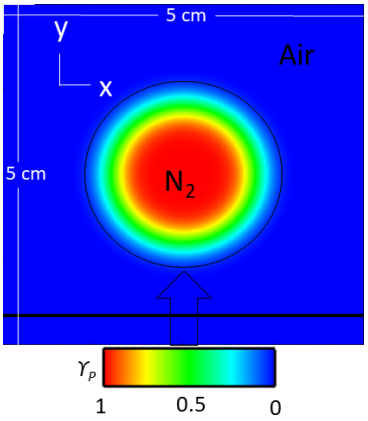

FIG. 3. Two-dimensional (2D) species pseudocolor representing all initial conditions for this work. Here the shock wave is traveling in the $+Y$ direction and the interface is considered as a 2-cm diameter cylinder of N_2 at $T = 2500$ K. The magnetic field, if present, may be parallel (along Y) or perpendicular (along X) to the direction of propagation of the shock and is not shown here. The image is centered about $y = 0$.

occurs at weak magnetic fields in ideal MHD, it is possible that even with resistivity effects a strong magnetic field is unnecessary to suppress the instability. The results for this study are shown in Sec. III B. Similar to Sec. III A, this section has $M = 1.66$ and $A = 0.79$.

The final parameter investigated within this work is the Mach number. The two previous studies explored the effects of the magnetic field, but it is also of interest to see how the hydrodynamics variables may affect the evolution of this interface in MHD. Sections III A and III B utilize $M = 1.66$, and so this study will expand the Mach numbers to include $M = 1.2$ and $M = 2.2$. These numbers were selected as they are within the range of our shock tube, and the postshock velocity increases by approximately 200 ms^{-1} with increasing M. This study will only consider the $B = 0$ G and $B = B_{\perp} = 500$ G cases. As this work seeks to study a shock-driven hydrodynamic instability in magnetohydrodynamics, it should be noted that the inclusion of MHD effects can alter the shock jump equations due to the addition of the magnetic pressure term [56]. However, the initially single directional magnetic fields presented here do not meaningfully change the postshock conditions. This was observed by looking at the postshock scalar fields for temperature and pressure, which vary up to 3% from the expected conditions, and the postshock velocities, which vary up to 2%. Therefore, the authors feel confident in comparing 500-G magnetic fields cases to the traditional RMI at different Mach numbers in this work.

When discussing the results, a naming convention becomes necessary in the face of such a wide parameter space. As such, the following naming convention will be used. Each case will be denoted in the following format: $M\#B_{\text{dir}}\#$, where $M\#$ indicates the Mach number and the # is replaced by a 1.2, 1.7, or 2.2 for a Mach number of 1.2, 1.66, or 2.2, respectively. The second half of the nomenclature represents the magnetic field. Here, dir can be either $\perp$ or $\parallel$ to represent a field perpendicular or parallel to the shock wave direction. The # will be either 10, 25, or 50 for a field of 100, 250, or 500 G. Lastly, there are cases where the magnetic field will be set to 0 to recover the traditional RMI and will be denoted by $B0$. For example, $M1.7B0$ stands for a case which considers a Mach number of 1.66 and no magnetic field.

III. RESULTS

For a traditional cylindrical RMI with these initial conditions, $M1.7B0$, significant RMI development occurs as early as $t = 0.5$ ms postshock. However, it is desirable for each case to be considered using a standard temporal scale, especially across the various Mach numbers. As such, a nondimensional time common in RMI literature will be used for all cases. This time, given in Eq. (11), is a function of time, the interface amplitude, and the shock wave transit speed or t, η_0, and w_i respectively. Since the interface is a cylinder, the interface amplitude is replaced by its diameter, and thus $\eta_0 = d$. Therefore, all simulation results will be presented using τ for consistency:

$$\tau = \frac{t w_i}{d}. \tag{11}$$

A. Magnetic field orientation

The first study presented in this work will compare the $M1.7B_{\perp}50$ and $M1.7B_{\parallel}50$ cases to the traditional RMI case denoted as $M1.7B0$. Figure 4 contains the species pseudocolor with respect to τ and has been annotated in order to aid discussion. At early time, $M1.7B0$ shows two large vortices and a thin bubble front. As the simulation progresses, this bubble front dissipates and the vortices begin mixing. By late time, the tight vortex structures have experienced significant mixing, leaving almost no pure plasma species. The most similar MHD RMI case is $M1.7B_{\parallel}50$, where the magnetic field is parallel to the shock direction. This case shows similar evolution at early time but with less developed vortices and a thicker bubble front. At midtime, large vortex structures have formed but exhibit less mixing and a larger area where the plasma species is preserved when compared to $M1.7B0$. There is also a morphological difference in the vortices, as tear-drop-like spikes form near the leading edge of the interface. At late time, the vortices and spikelike structures

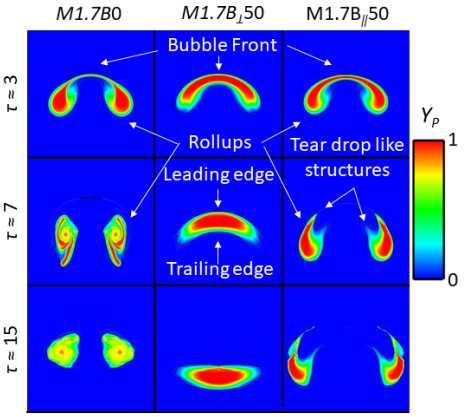

FIG. 4. Magnetic orientation study; pseudocolor of species for the $M1.7B0$, $M1.7B_{\perp}50$, and $M1.7B_{\parallel}50$ cases with respect to τ. The images are centered about y, respective to τ at $y(\tau \approx 3) = 3.11$ cm, $y(\tau \approx 7) = 7.64$ cm, and $y(\tau \approx 15) = 15.55$ cm.

have been stretched as the interface grows. However, there is a significant reduction in species fraction dissipation, which suggests a reduction in mixing with the surrounding gas.

The middle column shows results from $M1.7B_{\perp}50$. Immediately a difference can be seen between this case and the other two as early as $\tau \approx 3$. Here, a thick bubble front is present with almost no vortex development. By midtime, the morphology is significantly different than the other two cases. No vortex features are present; instead there is a thick bubble front structure. There is also significantly less mixing, with a strong concentration of pure plasma. At this time, the bubble front also exhibits a convex leading edge and a concave trailing edge. By late time, the configuration of these regions have reversed. That is, the interface has inverted itself. Similar to midtime, there is almost no change in the species pseudocolor to suggest additional mixing. Therefore, both magnetic field orientations show a decrease in qualitative mixing and RMI evolution when compared to the traditional RMI, with $M1.7B_{\parallel}50$ showing similar morphology with reduced qualitative mixing and $M1.7B_{\perp}50$ showing no discernible evidence of the RMI.

It is common when considering the RMI to try to quantify the mixing. However, this can be a challenge as one must determine the amount of mixed fluid versus the amount of entrainment in the system. The mixedness parameter, given in Eq. (12), is often used in RTI literature [57], and is considered as the ratio of the mixing half-width layer, h, to the half-width homogeneous mixing layer, h_{hom}, or simply the ratio of mixing to entrainment. These widths are functions of the mass fraction of the plasma species, Υ_P, where an overbar and $'$ denote an average and a fluctuating component respectively. The mixedness is bounded between 0, for a case in which no mixing has occurred, and 1, where two species have mixed completely. To calculate Ξ, the averages were taken in Y while the integrals were taken in X. This parameter is shown in Fig. 5. Since the qualitative evolution is indicative of mixing, it is expected that the more RMI-like evolution that is observed, the higher the mixedness as time advances. However, in Fig. 5, each case shows an initial decreasing mixedness. Just after the passage of the shock wave, the interface exhibits large-scale mixing, or entrainment, due to compression. However, as vorticity becomes active on the interface, a traditional RMI will experience greater small-scale mixing and the mixedness will trend towards turbulence. Conversely, more suppressed cases which do not experience small-scale mixing may either exhibit a shallow positive slope or stagnant mixedness behavior. Therefore, $M1.7B0$, or the traditional RMI, should exhibit the highest mixedness. From Fig. 5, this is indeed the case. It follows then that since $M1.7B_{\parallel}50$ is more similar to $M1.7B0$, it would have the second highest mixedness, while $M1.7B_{\perp}50$ has the least. From Fig. 4, it was expected that the mixing had stopped for $M1.7B_{\perp}50$ by $\tau \approx 7$ with only an interface inversion occurring between $\tau \approx 7$ and $\tau \approx 15$; indeed, the mixedness for this

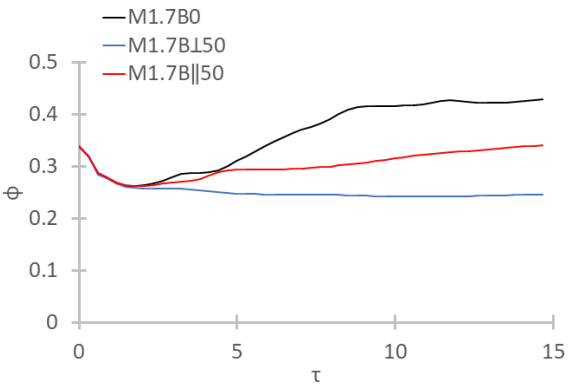

FIG. 5. Mixedness, Ξ, with respect to τ for the magnetic orientation study.

case is stagnant. The authors would like to note that while mixedness is a quantity sensitive to grid resolution, all simulations presented in this work share a resolution of 100 nodes per diameter. Therefore, while mixedness may scale with the resolution, the general trends are expected to hold so long as each simulation is compared on a fair grid. It should also be noted that the authors do not expect to be able to converge integral measurements in a 2D geometry, and thus to get reliable results one should run 3D simulations. Thus, the mixedness plots should be considered for their trends only:

$$\Phi = \frac{h}{h_{\text{hom}}} = 1 - \frac{\int_{-L}^{L} \overline{\Upsilon_P' \Upsilon_P'} dx}{\int_{-L}^{L} \overline{\Upsilon_P}(1 - \overline{\Upsilon_P}) dx}. \tag{12}$$

In order to understand the observed differences in both qualitative and quantitative mixing between the cases, one can look at the mechanism responsible for the evolution of the RMI, that is, vorticity. The vorticity is calculated using Eq. (13). When considering the effects of MHD waves, it is important to visualize the vorticity and explore whether that vorticity is causing mixing. To generate RMI mixing, the vorticity must act on the gradient of species. Thus, a new parameter was created by taking the magnitude of the species gradient and multiplying it by the magnitude of the in-plane vorticity, as shown in Eq. (14). This parameter, Ξ, is shown at late time in Fig. 6 alongside ω:

$$\vec{\omega} = \nabla \times \vec{u}\,, \tag{13}$$

$$\Xi = |\nabla \Upsilon_P||\vec{\omega}|. \tag{14}$$

In Fig. 6, ω is shown at times $\tau \approx 3$, 7, and 15, while Ξ is shown only at late time. For $M1.7B0$, the vorticity is very neatly organized with similar behavior to the corresponding species pseudocolor. It was previously discussed that the maximum vorticity will be deposited at two sites normal to the shock wave direction. Its also known that the vorticity will be advected by the MHD waves along the field lines. $M1.7B_{\parallel}50$ shows this through a stretched vortex field. The $M1.7B_{\parallel}50$ case has a vorticity field similar to $M1.7B0$, that is, two vortices at $\pm\pi/2$. However, the vorticity has been stretched and organized into layers as opposed to cores and can be seen to be acting over a larger area than the interface. The vorticity only appreciably intersects the interface on the outside perimeter of the leading edge near the tear-drop-like spikes. This stretched, less organized vortex field can explain both the stretching of the interface and the reduction in mixing.

The vorticity field in $M1.7B_{\parallel}50$ exhibits a stretched field as predicted by previous discussion; thus one might expect the perpendicular magnetic field to move the vorticity normal to the shock wave direction in $M1.7B_{\perp}50$, causing vortex competition. This would not only remove the vorticity

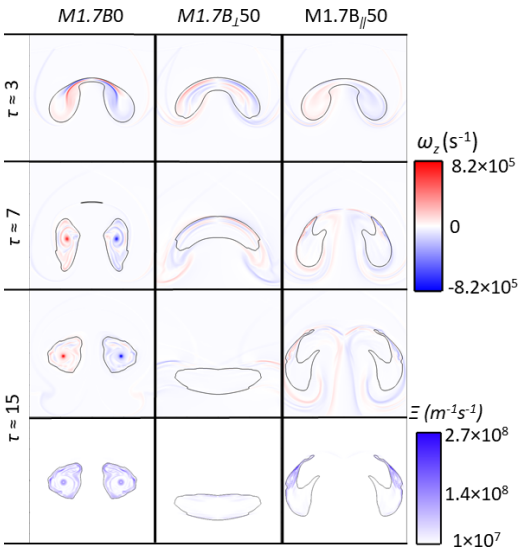

FIG. 6. Late-time pseudocolors for ω and Ξ for the magnetic orientation study. The images are centered about y, respective to τ at $y(\tau \approx 3) = 3.11\,\text{cm}$, $y(\tau \approx 7) = 7.64\,\text{cm}$, and $y(\tau \approx 15) = 15.55\,\text{cm}$.

from the interface faster than in $M1.7B_{\parallel}50$, which advects tangentially in such a way as to interact with the interface over a longer time, but it could cause vorticity to compete within the interface and potentially cancel. While vortex competition may also occur in a parallel field case, the lack of vortex stretching in the direction of the shock wave propagation in the perpendicular field may lead to greater vortex cancellation. In $M1.7B_{\perp}50$, the signs of vorticity have switched, that is, the positive vorticity is on the right of the interface and the negative on the left, suggesting vortex advection across the interface. The vorticity also appears to be weaker than in the other two cases, also suggesting some mechanism to reduce the total vorticity.

In an effort to illuminate the effects of the vorticity advection Ξ visualizes the interaction of vorticity and the species gradient, which is the source of mixing, and is shown in the second row of Fig. 6. $M1.7B0$ shows a Ξ field very similar to the vorticity and species. There is a strong Ξ core where the plasma mass fraction approaches one and the vorticity is the strongest, and layers of Ξ where vorticity works to mix the interface with the surrounding species, driving the species gradient to decay. The results of the stretched vorticity field in $M1.7B_{\parallel}50$ can also be seen in Ξ to cause mixing in the outer leading edges of the rollup structures. Here, moderate vorticity acts on a very strong species gradient, creating Ξ twice the magnitude experienced in $M1.7B0$. Despite its strength, Ξ only works on the outer edge of the interface, causing the interface to stretch but not mix to levels seen in $M1.7B0$.

In $M1.7B_{\perp}50$, Ξ is a full order of magnitude smaller than the other cases. Here, despite there being a large species gradient, that is almost no mixing has occurred, creating a large area with a steep species gradient. There is also almost no vorticity acting on the interface. In fact, the majority of the Ξ which can be seen in this case appears at the leading and trailing edges of the interface, the areas where the inversion is most apparent. This also explains why the vortex features do not exist in this case; there is no vorticity acting on the edges of the interface where the vortices would form.

To quantify the energy in the vorticity, enstrophy is used, calculated as shown in Eq. (15). Enstrophy is typically integrated across the entire simulation domain, as the enstrophy exists at the interface for a RMI and thus must be an accurate representation of the energy working to drive the instability. However, in MHD it has been shown that the vorticity advects, leaving the interface without mixing. As such, it is important to see what differences the area of integration can show for the enstrophy. This can be illuminated by Fig. 7. In this figure, two enstrophy values are plotted for

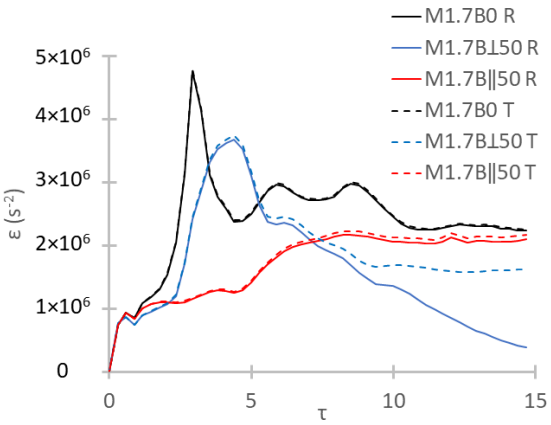

FIG. 7. The total and reduced area (local) enstrophy for the $M1.7B0$, $M1.7B_{\perp}5$, and $M1.7B_{\parallel}5$ cases.

$M1.7B0$, $M1.7B_{\parallel}50$, and $M1.7B_{\perp}50$. The first enstrophy value, the local enstrophy, is denoted by the case name with a succeeding R. To calculate this value, the integral in Eq. (15) is taken across the same reduced area shown in images, a 5-cm by 5-cm square centered about the interface. The other quantity, labeled with a T, implies the traditional enstrophy taken across the entire domain.

Comparing the reduced area enstrophy between cases, it can be seen that $M1.7B0$ has the most enstrophy, which can be expected as the traditional RMI exhibits the most mixing and the highest vorticity. $M1.7B_{\parallel}50$ has less enstrophy in early time but this steadily increases until it reaches levels similar to $M1.7B0$. Similar to the previous discussion, $M1.7B_{\perp}50$ shows an overall net decrease through time when compared to the other two cases. By late time, the local enstrophy tends to low levels as the vorticity is carried away from the interface. Since this is a large reduction in local enstrophy, it becomes necessary to consider the total enstrophy to see if the difference between the cases is due to the reduced area or the MHD effects. Here, it can be seen that the $M1.7B0$ and $M1.7B_{\parallel}50$ cases have similar enstrophy when compared to their reduced area values. In fact, it becomes difficult to see any difference for $M1.7B0$, which is to be expected as there is no magnetic field to carry the vorticity away. In the $M1.7B_{\perp}50$ case, some of the lost local enstrophy is recovered by integrating across the entire domain, but a significant reduction in total enstrophy is observed compared to $M1.7B0$ and $M1.7B_{\parallel}50$. Both MHD RMI cases exhibit less total enstrophy than the RMI, suggesting that the MHD waves cause vortex competition with the greatest effect in $M1.7B_{\perp}50$ due to the normal direction of the Alfvén velocity.

The magnitudes of integral mixing measurements, such as mixedness and enstrophy, are grid dependent and are difficult to achieve convergence with a limited resolution [58]. Previous work using a similar ALE code has shown that a resolution of over 1400 zones/diameter is necessary for convergence of enstrophy in inviscid simulations of a shock-cylinder problem like that presented here [59]. Despite this requirement for high-resolution simulations, experimental comparisons have shown that even low-resolution studies capture the morphology of the interface well and reproduce the effect of changing the Atwood number [60]. In addition, 2D simulations show similar results to 3D simulations for early time but they overpredict vorticity by approximately 10% at late times [61]:

$$\epsilon = \int \vec{\omega} \cdot \vec{\omega} \, dA \tag{15}$$

In an effort to explain why the interface mixing has differed from the traditional RMI in the MHD cases, the vorticity has been studied. However, the movement of the vorticity, highlighted by the reduced area enstrophy, can offer a complicated story to consider. In an effort to capture the relationship between the species gradient and vorticity, Ξ was used to give a qualitative metric at a

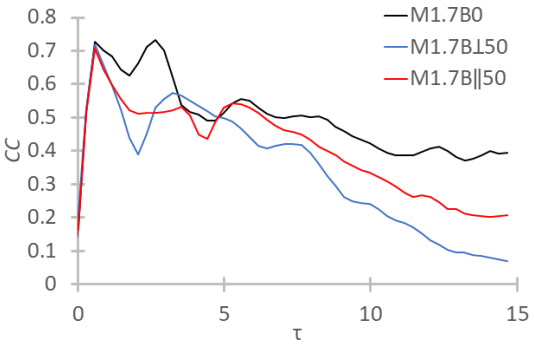

FIG. 8. The correlation coefficient with respect to τ for the magnetic orientation study.

single time in Fig. 6. To try to quantify this over time, a correlation coefficient was created to relate the species gradient and vorticity as shown in Eq. (16). In this equation, the numerator is similar to Ξ and is in fact the origin of this parameter.

The correlation coefficient relating the species gradient and vorticity, here on out referred to simply as the correlation coefficient, is plotted in Fig. 8. $M1.7B0$ exhibits the highest correlation between vorticity and the species gradient throughout time. However, this correlation decreases with respect to time. This is due to the nature of mixing; as vorticity acts on the interface, it breaks down the species gradient and thus tends toward a lower correlation. The correlation for $M1.7B_{\parallel}50$ also shows similar behavior to $M1.7B0$, although less correlated through time. As opposed to mixing, the decrease of the correlation coefficient for $M1.7B_{\parallel}50$ can be attributed to the vorticity advection away from the interface. Here, the vorticity acts to elongate the interface but does not cause mixing everywhere. $M1.7B_{\perp}50$ shows significantly less correlation at late time than the other cases. This is due to the vorticity motion along the magnetic field lines rather than mixing, which drops the correlation coefficient to a value lower than 0.1:

$$CC = \frac{\langle |\nabla \Upsilon_P| |\vec{\omega}| \rangle}{\sqrt{\langle |\nabla \Upsilon_P|^2 \rangle \langle |\vec{\omega}|^2 \rangle}}. \tag{16}$$

The following sections will only consider the species and vorticity pseudocolors qualitatively and the correlation coefficient and the mixedness plots quantitatively. Through the observation of these parameters, one can infer the others. For instance, along with the knowledge presented in this section, one can infer the interaction of the vorticity with the species gradient, Ξ, by observing the mixedness and the vorticity field. If the mixedness increases and there is vorticity present at the interface, then it would be expected Ξ would show the interaction of the species gradient and the vorticity. The enstrophy in Fig. 7 was used to show that the energy in the vorticity decreases in the presence of a magnetic field and that one can quantify the energy of the vorticity acting on the interface by considering a small area about the interface. However, when considering the species pseudocolor and the mixedness, one can infer the species gradient behavior through time. Thus, any differences between the mixedness and the correlation coefficient must be due to the behavior of the vorticity, which can be shown via the vorticity psuedocolor.

B. Magnetic field strength

The previous section showed that both the presence of a magnetic field and the orientation of said field effects the evolution of the MHD RMI. Therefore, it is of interest to vary the strength of the initialized magnetic field, which controls the dispersion of the MHD waves via the Alfvén velocity. Thus, this section includes both the parallel and perpendicular magnetic configurations and varies them from 100, 250, and 500 G. Figure 9 shows species pseudocolor plots for the parallel field configuration. It is expected that the weaker the magnetic field, the more similar to the traditional

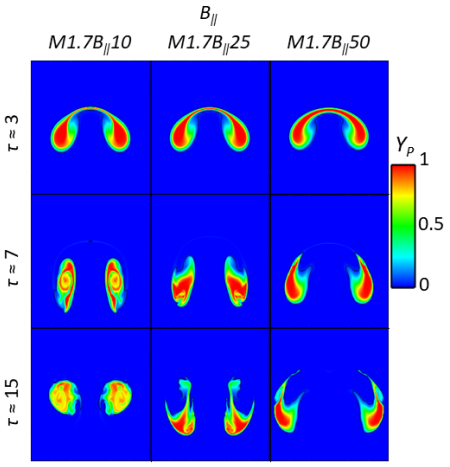

FIG. 9. Magnetic strength study. Pseudocolor of species for the parallel magnetic field cases with respect to τ. The images are centered about y, respective to τ at $y(\tau \approx 3) = 3.11\,\text{cm}$, $y(\tau \approx 7) = 7.64\,\text{cm}$, and $y(\tau \approx 15) = 15.55\,\text{cm}$.

RMI the instability will be. The weaker magnetic fields will remove vorticity from the interface at a slower rate, allowing more time for the baroclinic vorticity to cause mixing. It was previously shown that at early times $M1.7B_{\parallel}50$ was similar to $M1.7B0$ and it follows that both $M1.7B_{\parallel}10$ and $M1.7B_{\parallel}25$ will exhibit vortexlike features. In fact, at $\tau \approx 3$ these two cases look very similar to $M1.7B0$. However, by midtime the field strength effects become noticeable. Here, $M1.7B_{\parallel}10$ shows organization similar to the traditional RMI but with a much tighter interface and no spikelike structure emerging on the leading edge. This organization continues through late time with tight vortices that have more pure plasma species than the traditional case. Thus, while $M1.7B_{\parallel}10$ is very similar to $M1.7B0$, it still has reduced mixing.

$M1.7B_{\parallel}25$ shows a similar instability to $M1.7B_{\parallel}50$, and at midtime tear-drop-like spikes are developed. However, in $M1.7B_{\parallel}25$ these spikes are on the inner leading edge. This trend continues into late time with the elongation of these spikes and the preservation of the plasma species. That is, as the parallel magnetic field strength is increased, the RMI mixing is further decreased.

Tabling the discussion on the parallel field for a moment, consider Fig. 10. This figure contains a study similar to that in Fig. 9 but for the perpendicular field. Similar to the parallel field study, the early-time weaker magnetic field cases show stronger similarities to $M1.7B0$. That is, $M1.7B_{\perp}10$ and $M1.7B_{\perp}25$ both have clear vortex features and a thin bubble front. However, with increasing magnetic field strength, the vortices are reduced in size and the bubble front is thickened. Unlike $M1.7B_{\parallel}10$, $M1.7B_{\perp}10$ shows significant departure from the RMI by midtime. Here $M1.7B_{\perp}10$ shows flattened vortex structures connected by a diffusive bubble front, a component which is negligible in $M1.7B0$. At late time, in $M1.7B_{\perp}10$ the bubble front prevails, albeit stretched and diffusive. The vortex structures have thinned as mixing has worked to diffuse the plasma species, but the morphology and mixing is significantly different even in the presence of this weak perpendicular magnetic field. This evolution is as different from the traditional RMI as the evolution in $M1.7B_{\perp}50$. However, instead of obvious suppression, this interface appears very diffusive and stretched. Qualitatively it is difficult to claim that $M1.7B_{\perp}10$ is suppressed compared to $M1.7B0$, although it is clearly effected by the magnetic field.

$M1.7B_{\perp}25$ is more similar to $M1.7B_{\perp}50$, exhibiting a strong bubble front at midtime. Unlike $M1.7B_{\perp}50$, $M1.7B_{\perp}25$ has significant curvature, which resembles the mushroom shape in $M1.7B_{\perp}10$. The vortices which were present at early time have almost vanished, with thin fingerlike structures shown peeling back at midtime. At late time, these structures are gone and only a sharp

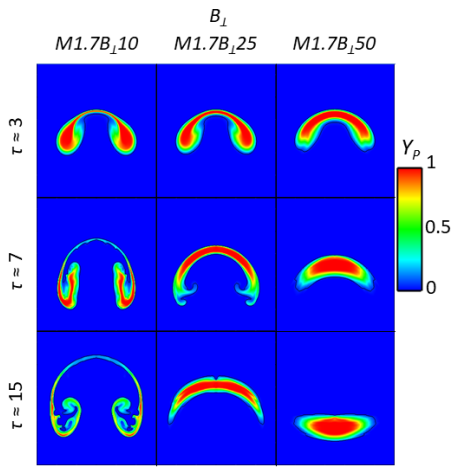

FIG. 10. Magnetic strength study. Pseudocolor of species for the perpendicular magnetic field cases with respect to τ. The images are centered about y, respective to τ at $y(\tau \approx 3) = 3.11$ cm, $y(\tau \approx 7) = 7.64$ cm, and $y(\tau \approx 15) = 15.55$ cm.

point remains on either side of the interface. At this time, $M1.7B_{\perp}25$ has a significant reduction in mixing from $M1.7B_{\perp}10$ though more curvature than $M1.7B_{\perp}50$. While $M1.7B_{\perp}25$ has not inverted its leading and trailing edges, the fingerlike structures which formed in place of vortices have seemingly been inverted. This is likely the same mechanism that works to invert the interface in $M1.7B_{\perp}50$, albeit weaker due to the weaker magnetic field.

Figure 11 shows the mixedness for the magnetic field strength study. Similar to the qualitative mixing in Fig. 9, $M1.7B_{\parallel}10$ shows the most similar mixedness to $M1.7B0$. Both cases steady out around $\tau \approx 7$; however, $M1.7B_{\parallel}10$ shows a reduction throughout time. Interestingly, the 250- and 500-G fields exhibit similar mixedness history for the parallel and perpendicular fields, respectively. This indicates that while increasing the strength of a magnetic field may change the morphology of the species and vorticity fields, there may be a limit to its effect on mixing. That is, the MHD waves are a function of the Alfvén velocity, which in turn is a function of the magnetic field strength. Despite any macroscopic changes to the interface, the mixedness suggests that the maximum suppression, within the range of these magnetic field strengths, can happen as low as 250 G for either field orientation with no additional effect made apparent by doubling the magnetic field strength.

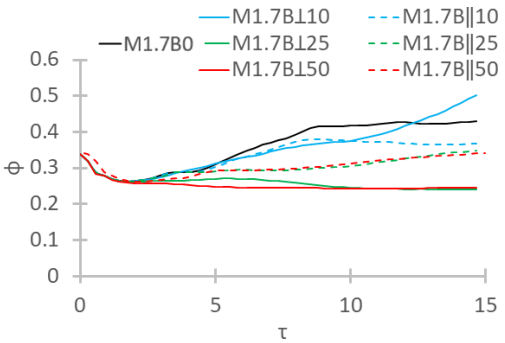

FIG. 11. The mixedness for the magnetic strength study. Here $B0$ is included to highlight the effects of the magnetic field.

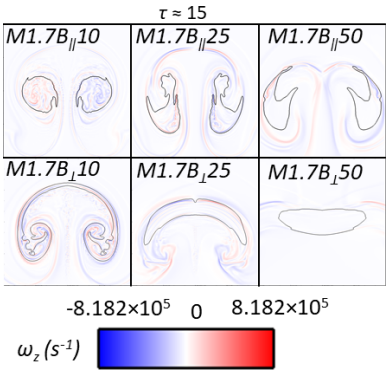

FIG. 12. Late-time vorticity field for the magnetic strength study. The images are centered about $y(\tau \approx 15) = 15.55\,\text{cm}$.

Perhaps the most interesting case in this section is $M1.7B_{\perp}10$. Figure 10 shows a significantly stretched interface throughout time. This is the only case in which a thin bubble front connects to vortex features at late times. Qualitatively, it is difficult to know if the regions where the plasma species fraction is more concentrated have a greater area than other cases, but the mixedness seems to suggest that $M1.7B_{\perp}10$ has superior mixing even compared to the traditional RMI. This is because the vortex field is stretched and weakened by the magnetic field, stretching the interface without breaking down the bubble front or organizing vortices fully. This creates a larger mixing surface area, thus leading to greater mixedness or a larger ratio of mixing to entrainment. This condition may be temporary, as the bubble front separates with time, leading to a mixedness more similar to the other cases at late times.

To understand the qualitative and quantitative mixing differences in Figs. 9, 10, and 11, the late time vorticity field is shown in Fig. 12. For both fields, the organization of the vortex field increasingly breaks down with stronger field strengths. As discussed earlier, this is because the vorticity is being carried away from the interface along the magnetic field lines eventually causing vortex competition. For the parallel cases, the vorticity field takes on a mushroom shape with strongly organized vortex cores. For $M1.7B_{\parallel}10$, the magnetic field is weak enough that the majority of the vorticity is not removed from the interface and thus causes RMI mixing. As the magnetic field strength increases, the vorticity advects further away from the interface. In $M1.7B_{\parallel}25$, the organized vorticity seems to form more sheetlike structures and is pushed into the stem region, causing the inner tear-drop-like spikes to form. This vorticity is moved further away in $M1.7B_{\parallel}50$. Evidence of the inner spike can be seen more clearly here; however, as the vorticity is pushed away further to the outside of the interface, the outer leading-edge spike is more prevalent.

The mushroom shape of the vorticity field, noticeable in the parallel cases, is also apparent in the weak perpendicular cases. For $M1.7B_{\perp}10$, the field is very similar to $M1.7B_{\parallel}10$. However, here the vorticity movement is clearly more normal to the direction, causing the vorticity to create a large diffusive interface which may indicate more mixing. The vorticity is also less organized with more visible layers. Comparing these two cases, it is also noticeable that $M1.7B_{\perp}10$ has more positive and negative vorticity interaction than in $M1.7B_{\parallel}10$, which has more organized strong positive vorticity on the left-hand side and negative on the right. In $M1.7B_{\perp}25$, the mushroom-shape vorticity field becomes stunted in the direction of shock transit, with the vorticity being pushed to the side by the perpendicular magnetic field. Here, more negative vorticity can be seen on the left, while stronger positive vorticity is apparent on the right, having already alternated sides due to the traverse MHD waves. In this case, a complex interaction of positive and negative vorticity can be seen near the bottom side of the interface. Earlier in time, these spike structures appeared like roll-ups which eventually took fingerlike shapes at midtime (see $\tau \approx 7$ in Fig. 10) and have disappeared by late

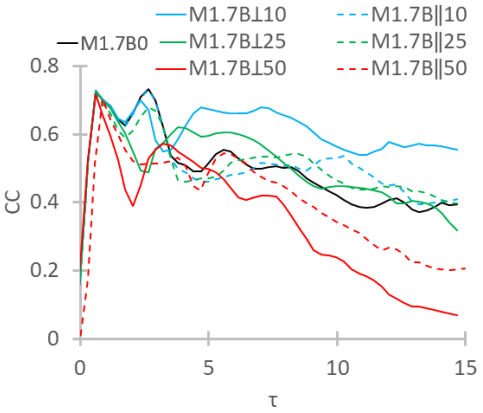

FIG. 13. The correlation coefficient, given as Eq. (16), for the magnetic strength study.

time. It is likely this vortex interaction is responsible for the apparent reduction in organization of this structure and that this same interaction is responsible for the late time inversion of the $M1.7B_{\perp}50$ case.

The correlation coefficient for the magnetic field study is presented in Fig. 13. Similarly to what was observed in Fig. 11, $M1.7B_{\perp}10$ has a higher correlation due to the stretched species and vorticity fields. That is, the species gradient acts over a larger area and at a greater magnitude than $M1.7B0$, driving up both mixedness and the correlation between the fields. Aside from $M1.7B_{\perp}10$, it might be expected that $M1.7B0$ is the most correlated considering the absence of MHD effects. However, the correlation coefficient is dependent upon the magnitude of vorticity acting on the magnitude of the species gradient. Therefore, if a case were to exceed the correlation of the traditional RMI, it would need either greater vorticity at the interface or a larger, longer lasting species gradient. It has been shown explicitly that in the presence of a magnetic field the vorticity moves away from the interface in Sec. III A, and Fig. 12 shows that even a weak magnetic field can affect the vortex field. Therefore, the increased correlation in $M1.7B_{\perp}10$ is due to the larger interface with steep species gradients.

$M1.7B_{\parallel}10$ and $M1.7B_{\parallel}25$ have a similar correlation to $M1.7B0$. This is easy to explain for $M1.7B_{\parallel}10$, which is the most similar case to $M1.7B0$, both through qualitative mixing and in its vortex field. $M1.7B_{\parallel}25$ gets its large correlation then from its species gradient. Figure 10 shows a relatively unmixed stretched interface, with a large gradient of species in the inner leading-edge spikes. Looking at Fig. 12, the majority of the strong vorticity acting on the interface acts on this region, causing the mixedness seen in Fig. 11. Thus, the large correlation coefficient is due to the interaction of this large gradient with its vorticity, whereas the correlation coefficient for $M1.7B0$ is due to the large vorticity acting on the species gradient. The remaining cases act as one may predict. That is, neglecting $M1.7B_{\perp}10$, as the magnetic field strength is increased the correlation coefficient is decreased, and the perpendicular field cases exhibit less correlation than their parallel field counterparts.

C. Incident shock wave strength

In the previous section, the magnetic field strengths and orientations were varied for the cylindrical MHD RMI with $M = 1.66$. This Mach number provides the pressure gradient necessary to deposit baroclinic vorticity. It is common to vary the Mach number in literature to understand how an interface might evolve due to different impulsive accelerations. This is important as Richtmyer's linear model says that the amplitude growth of the RMI instability is proportional to the shock jump velocity [12]; thus, increasing the Mach number leads to a stronger instability. In addition to

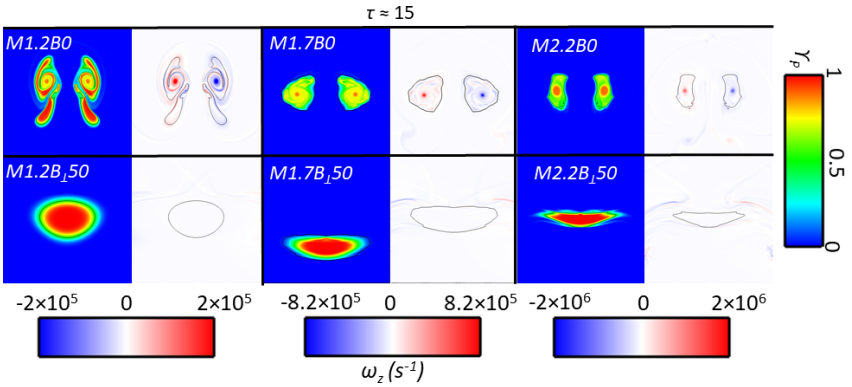

FIG. 14. The late-time species and vorticity plots for the incident shock wave strength study. The species pseudocolors are all on the same scale shown on the right of the image while the vortices are Mach number specific and shown below each group. The images are centered about y, respective to M at $y(M = 1.2) = 7.60$ cm, $y(M = 1.7) = 15.55$ cm, and $y(M = 2.2) = 19.40$ cm.

creating a stronger instability, the Mach number also determines postshock conditions that influence the evolution of the interface (e.g., density). In the MHD RMI, the density also effect the MHD wave velocities. Thus, two additional Mach numbers will be studied here: $M = 1.2$ and $M = 2.2$. These Mach numbers were selected for their incremental increase in the shock jump velocity by $\approx$200 ms^{-1}. This study is different from those presented in Secs. III A and III B, as it is not a study on MHD parameters alone, but rather on a traditional hydrodynamic variable which has MHD consequences. Both the classic RMI, $B = 0$, and a perpendicular magnetic field of 500 G, $B = B_\perp = 500$ G, will be presented for each Mach number. The perpendicular magnetic field was selected as it shows the greatest difference from the RMI case.

Figure 14 shows the species and the vorticity pseudocolors at late time, $\tau \approx 15$. The traditional RMI cases, shown in the top row of Fig. 14, exhibit classic RMI behavior, which has been described in other works. Therefore, for brevity it will only be said that with increasing Mach number more baroclinic vorticity is deposited on the interface driving mixing at a faster rate. Hence $M2.2B0$ evolves faster and exhibits more mixing and stronger vorticity than either $M1.7B0$ or $M1.2B0$. The cases all share similar organization in the species and vorticity fields.

Moving on to consider the MHD RMI, the magnetic field cases are shown in the second row of Fig. 14. At late time, $M1.2B_\perp50$ shows a large very round interface with almost no mixing. Here, the interface has been slightly compressed but otherwise undisturbed. Its organization is very similar to the initial conditions (Fig. 3) with a thick, clear, and unmixed diffusion layer. Looking at its vortex field, one can see almost no vorticity near the surface of the interface, and indeed what vorticity is present in this image is low enough to be incomparable when considering the magnitude of vorticity in $M1.2B0$. As the Mach number increases, the MHD RMI interfaces exhibit greater compression. In addition to this compression, it appears as though the greater Mach number also leads to more mixing of the diffusion layer. For example, when considering $M1.7B_\perp50$, the interface shows more compression than its low-Mach-number neighbor. The high-Mach-number case, $M2.2B_\perp50$, shows a highly compressed interface with significantly less mixing and no resemblance to its magnetic-field-free counterpart, $M2.2B0$. The vorticity field of both these cases is similar in that they exhibit negative and positive layers of vorticity on the left and right sides of the interface respectively and neither case appears to have any vorticity active on the interface.

To understand how this has occurred, one should remember the mechanisms which work to remove vorticity are a function of the Alfvén velocity. While the magnetic field in these cases is initialized at 500 G, the Alfvén velocity also has the density of the species in the denominator. Thus, there are two effects to consider for a larger Mach number. First off, the postshock density is

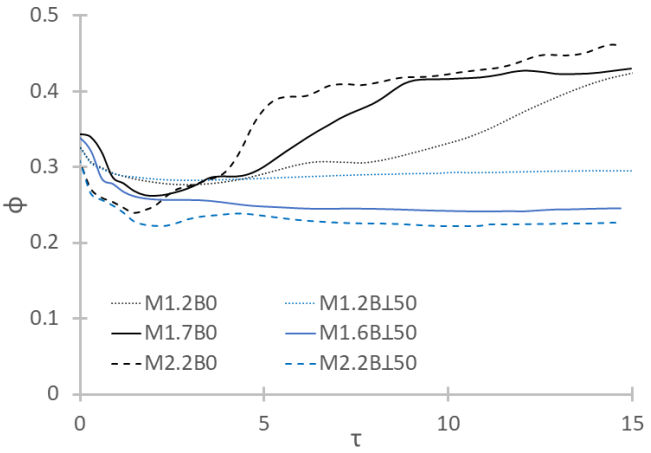

FIG. 15. The mixedness for the incident shock-wave study. Small dashed lines indicate $M = 1.22$, solid lines indicate $M = 1.66$, and large dashed lines indicate $M = 2.2$, while black represents cases without a magnetic field and blue represents cases with a perpendicular magnetic field of 500 G.

proportional to the Mach number while the Alfvén velocity is inversely proportional to the density. Since the magnetic field is also a function of the density of the perfect conductor, Eq. (6), the Alfvén velocity then goes as $\approx\rho^{1/2}$, meaning that V_A then increases with increasing Mach number. Of course, the higher Mach number will also deposit a higher vorticity at the interface. Thus, higher Mach number cases will have stronger vorticity deposition that acts on the interface for a shorter amount of time.

Figure 15 shows the mixedness for the Mach number study. The nonmagnetic cases (black lines) show greater mixing with increasing Mach number as expected for the RMI. However, in the presence of a magnetic field, the higher Mach numbers exhibit lower mixedness. It was observed that $M2.2B_\perp 50$ is more compressed and exhibits a smaller diffusion layer than the other cases. Again, the mixedness is the ratio of mixing to entrainment. The area of entrainment between the MHD RMI cases is similar but as the stronger Mach number cases have greater Alfvén velocity there is less time for the vorticity to act on them and cause mixing. This, paired with a smaller diffusion layer, leads to a reduced mixing width, which in turn leads to less mixedness. Therefore, despite the observed interface compression in Fig. 14, $M2.2B_\perp 50$ exhibits less mixedness than $M1.7B_\perp 50$, which in turn exhibits less then $M1.2B_\perp 50$.

Finally, Fig. 16 shows the correlation coefficient for the Mach number study. Considering only the traditional RMI cases, it is expected that the higher the Mach number, the lower the correlation due to mixing, driving the species gradient to zero. This can be seen in Fig. 16, where $M1.2B0$ has the highest correlation coefficient and $M2.2B0$ has the lowest of the classic RMI cases. For the MHD RMI cases, an increasing correlation is observed with increasing Mach number and the $M1.2B_\perp 50$ shows the smallest correlation, for all cases, at late time. From the qualitative evidence, this makes sense: The vorticity deposited is simply too weak to cause mixing and does not remain near the interface, thus driving the correlation coefficient down.

$M2.2B_\perp 5$ exhibits the greatest correlation of the MHD RMI cases. This is due to the large magnitude of vorticity deposited at the interface. The vorticity is advected via the MHD waves but acts over a larger area and at a greater magnitude everywhere than its weaker Mach number counterparts. Therefore, while stronger baroclinic vorticity is able to further compress the interface, it is also advected more quickly over a greater area and at a higher magnitude. This can be seen by looking at the vortex fields for the MHD RMI cases in Fig. 14. $M2.2B_\perp 50$ exhibits the largest vortex field at the highest magnitude despite its higher vortex advection. Similarly, the vortex field in $M1.7B_\perp 50$ covers a larger area at a stronger magnitude than $M.12B_\perp 50$ but is still weaker than

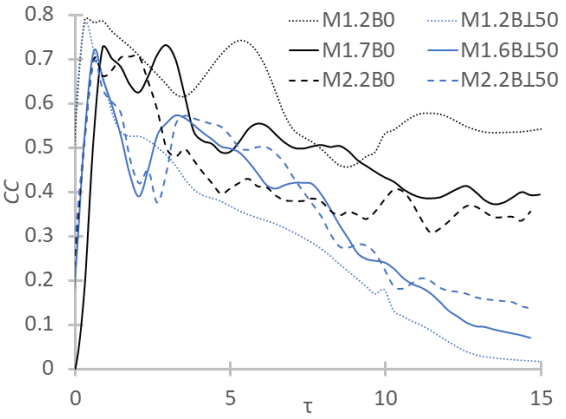

FIG. 16. The correlation coefficients for the incident shock wave study. Small dashed lines indicate $M = 1.22$, solid lines indicate $M = 1.66$, and large dashed lines indicate $M = 2.2$, while black represents cases without a magnetic field and blue represents cases with a perpendicular magnetic field of 500 G.

$M2.2B_{\perp}50$. Thus, despite there being little to no vorticity acting on the interface in any of the MHD RMI cases, there is increasingly more, with higher Mach numbers leading to an increased correlation coefficient. However, each of the MHD RMI cases exhibit far less correlation than their classic RMI counterparts.

IV. CONCLUSIONS

This work studied the cylindrical MHD RMI by varying the magnetic field orientation, magnetic field strength, and the incident shock wave Mach number (acceleration strength). The cylindrical interface was selected as its evolution is independent of the orientation of either the shock wave or the magnetic field direction. Instead, the evolution depends only on the orientation of the shock transit direction relative to the magnetic field. The magnetic field parameters were selected to explore their effects on vorticity advection caused by MHD waves, while the Mach number was selected to explore how increasing baroclinic vorticity deposition may effect the growth of the MHD RMI. It was shown that interface mixing is a function of the amount of vorticity deposition, the rate at which vorticity is advected, and the advection direction via Alfvén waves. This leads to a rich parameter space where some counterintuitive results are found in mixing measures. To understand the parameter space, the simulations were observed qualitatively via species and vorticity fields and quantitatively through mixedness, enstrophy, and the correlation coefficient of the vorticity and species gradient. It was found that in general the presence of the magnetic field suppresses RMI-like evolution by the advection of vorticity, with a stronger field and preferential field orientation, resulting in greater suppression. Overall, it was shown that interface mixing is a function of the amount of vorticity deposition, the rate at which it is advected, and the direction it is advected by Alfvén waves.

Expanding upon results found in literature, it was shown here that the presence of either a perpendicular or parallel magnetic field in the MHD RMI suppresses RMI evolution, with a perpendicular magnetic field showing less mixedness and significantly reduced RMI morphology compared its parallel field counterpart. This is because in the presence of a magnetic field the whole of the deposited baroclinic vorticity, which drives the evolution in the RMI, no longer remains on the density gradient. This interaction, shown by the species-gradient-vorticity correlation, can be seen to be significantly reduced for the MHD RMI cases when compared to the traditional RMI. The differences in field orientation are further highlighted by the vorticity field and enstrophy. The vorticity is stretched significantly in the direction of the magnetic field, and hence the parallel

field stretches the vorticity along the shock wave direction. Enstrophy versus time curves, for all enstrophy and enstrophy, only near the interface show that both orientations result in lower total enstrophy but that the perpendicular orientation has much lower enstrophy near the interface. Furthermore, vorticity is able to traverse the interface rapidly in the perpendicular field orientation, allowing positive and negative vorticity from opposite sides of the interface to interact and compete, diminishing the enstrophy.

As the magnetic fields are the driving mechanism for the vorticity transport, it follows then that as the magnetic field strength increases so does the suppression of the RMI evolution. However, by examining magnetic fields of 100, 250, and 500 G in both orientations, two nonobvious effects were observed. First, there appears to be some limit to the effectiveness of the magnetic field on mixing. That is, for both field orientations, increasing the magnetic field from 250 to 500 G did not significantly affect the mixedness. However, the vorticity and species fields displayed differences in morphology. Second, a competing effect was observed for the perpendicular field of 100 G. Here, the magnetic field was unable to remove the vorticity from the interface but instead moved it in such a way as to cause significant morphological differences. This interface appears much more diffusive and exhibits higher mixedness and correlation than any other case with $M = 1.66$. This implies that while strong fields have been shown to suppress the RMI, there may be a regime where magnetic fields can be used to redistribute vorticity through an interface and increase mixing. This effect is likely unique to the perpendicular orientation and the cylindrical interface.

While the magnetic fields drive the MHD effects, the Mach number drives the hydrodynamics, and exploring the initial Mach number in this work revealed another competing effect. Its known that for the RMI, an increasing Mach number leads to increased interface mixing due to the increased baroclinic vorticity deposition. However, the opposite was observed for the MHD RMI. Qualitatively, the higher Mach number cases further compressed the interface in the MHD RMI. However, this actively drove down mixedness by compressing the diffusion layer, the area where mixing could occur. While the stronger deposited vorticity worked to compress the interface, it was advected away by higher Alfvén velocities, due to the higher postshock density. Despite this, it was also shown that the stronger vorticity deposition resulted in a more correlated but unmixed interface. Thus, the higher Mach number cases exhibited less mixedness and higher vortex advection in MHD.

This work has shown that interface mixing is a function of the amount of vorticity deposition, the rate at which it is advected, and the direction it is advected by Alfvén waves. This leads to a rich parameter space where some counterintuitive results are found in mixing measures. Further simulations are planned to explore these results further and study the MHD RMI with extended MHD effects, resistivity, and two-fluid modeling and in 3D. The authors of this paper are also planning to investigate the parameters shown within this work through experiments planned at the University of Missouri Fluid Mixing and Shock Tube Laboratory.

ACKNOWLEDGMENTS

The authors would like to thank Los Alamos National Laboratory for the computational time and for summer student support to conduct this work. The authors would also like to thank the Stewardship Science Academic Alliances for their support via Grant No. DE-NA0003345.

[1] T. Sano, K. Nishihara, C. Matsuoka, and T. Inoue, Magnetic field amplification associated with the Richtmyer-Meshkov instability, Astrophys. J. **758**, 126 (2012).

[2] T. Sano, T. Inoue, and K. Nishihara, Critical Magnetic Field Strength for Suppression of the Richtmyer-Meshkov Instability in Plasmas, Phys. Rev. Lett. **111**, 205001 (2013).

[3] M. Hohenberger, P.-Y. Chang, G. Fiksel, J. Knauer, R. Betti, F. Marshall, D. Meyerhofer, F. Séguin, and R. Petrasso, Inertial confinement fusion implosions with imposed magnetic field compression using the omega laser, Phys. Plasmas **19**, 056306 (2012).

[4] M. R. Gomez, S. A. Slutz, A. B. Sefkow, D. B. Sinars, K. D. Hahn, S. B. Hansen, E. C. Harding, P. F. Knapp, P. F. Schmit, C. A. Jennings *et al.*, Experimental Demonstration of Fusion-Relevant Conditions in Magnetized Liner Inertial Fusion, Phys. Rev. Lett. **113**, 155003 (2014).

[5] A. B. Sefkow, S. Slutz, J. Koning, M. Marinak, K. Peterson, D. Sinars, and R. Vesey, Design of magnetized liner inertial fusion experiments using the z facility, Phys. Plasmas **21**, 072711 (2014).

[6] P. Y. Chang, G. Fiksel, M. Hohenberger, J. P. Knauer, R. Betti, F. J. Marshall, D. D. Meyerhofer, F. H. Séguin, and R. D. Petrasso, Fusion Yield Enhancement in Magnetized Laser-Driven Implosions, Phys. Rev. Lett. **107**, 035006 (2011).

[7] S. Slutz, M. Herrmann, R. Vesey, A. Sefkow, D. Sinars, D. Rovang, K. Peterson, and M. Cuneo, Pulsed-power-driven cylindrical liner implosions of laser preheated fuel magnetized with an axial field, Phys. Plasmas **17**, 056303 (2010).

[8] S. A. Slutz and R. A. Vesey, High-Gain Magnetized Inertial Fusion, Phys. Rev. Lett. **108**, 025003 (2012).

[9] S. Chandrasekhar, *Hydrodynamic and Hydromagnetic Stability* (Dover Publications, Mineola, New York, 1981).

[10] J. Kane, R. Drake, and B. Remington, An evaluation of the Richtmyer-Meshkov instability in supernova remnant formation, Astrophys. J. **511**, 335 (1999).

[11] G. Taylor, The instability of liquid surfaces when accelerated in a direction perpendicular to their planes. I, Proc. R. Soc. London, Ser. A **201**, 192 (1950).

[12] R. D. Richtmyer, Taylor instability in shock acceleration of compressible fluids, Commun. Pure Appl. Math. **13**, 297 (1960).

[13] E. Meshkov, Instability of the interface of two gases accelerated by a shock wave, Fluid Dyn. **4**, 101 (1969).

[14] H. F. Robey, J. Kane, B. Remington, R. Drake, O. Hurricane, H. Louis, R. Wallace, J. Knauer, P. Keiter, D. Arnett *et al.*, An experimental testbed for the study of hydrodynamic issues in supernovae, Phys. Plasmas **8**, 2446 (2001).

[15] C. Niederhaus and J. W. Jacobs, Experimental study of the Richtmyer-Meshkov instability of incompressible fluids, J. Fluid Mech. **485**, 243 (2003).

[16] P. Chapman and J. Jacobs, Experiments on the three-dimensional incompressible Richtmyer-Meshkov instability, Phys. Fluids **18**, 074101 (2006).

[17] D. Ranjan, J. Niederhaus, B. Motl, M. Anderson, J. Oakley, and R. Bonazza, Experimental Investigation of Primary and Secondary Features in High-Mach-Number Shock-Bubble Interaction, Phys. Rev. Lett. **98**, 024502 (2007).

[18] C. Tomkins, K. Prestridge, P. Rightley, M. Marr-Lyon, P. Vorobieff, and R. Benjamin, A quantitative study of the interaction of two Richtmyer-Meshkov-unstable gas cylinders, Phys. Fluids **15**, 986 (2003).

[19] C. Tomkins, B. Balakumar, G. Orlicz, K. Prestridge, and J. Ristorcelli, Evolution of the density self-correlation in developing Richtmyer-Meshkov turbulence, J. Fluid Mech. **735**, 288 (2013).

[20] G. Orlicz, B. Balakumar, C. Tomkins, and K. Prestridge, A Mach number study of the Richtmyer-Meshkov instability in a varicose, heavy-gas curtain, Phys. Fluids **21**, 064102 (2009).

[21] B. Motl, J. Oakley, D. Ranjan, C. Weber, M. Anderson, and R. Bonazza, Experimental validation of a Richtmyer-Meshkov scaling law over large density ratio and shock strength ranges, Phys. Fluids **21**, 126102 (2009).

[22] C. Long, V. Krivets, J. Greenough, and J. Jacobs, Shock tube experiments and numerical simulation of the single-mode, three-dimensional Richtmyer-Meshkov instability, Phys. Fluids **21**, 114104 (2009).

[23] M. Jones and J. Jacobs, A membraneless experiment for the study of Richtmyer-Meshkov instability of a shock-accelerated gas interface, Phys. Fluids **9**, 3078 (1997).

[24] C. Weber, N. Haehn, J. Oakley, D. Rothamer, and R. Bonazza, Turbulent mixing measurements in the Richtmyer-Meshkov instability, Phys. Fluids **24**, 074105 (2012).

[25] J. McFarland, D. Reilly, S. Creel, C. McDonald, T. Finn, and D. Ranjan, Experimental investigation of the inclined interface Richtmyer-Meshkov instability before and after reshock, Exp. Fluids **55**, 1640 (2014).

[26] D. Reilly, J. McFarland, M. Mohaghar, and D. Ranjan, The effects of initial conditions and circulation deposition on the inclined-interface reshocked Richtmyer-Meshkov instability, Exp. Fluids **56**, 168 (2015).
[27] J. A. McFarland, D. Reilly, W. Black, J. A. Greenough, and D. Ranjan, Modal interactions between a large-wavelength inclined interface and small-wavelength multimode perturbations in a Richtmyer-Meshkov instability, Phys. Rev. E **92**, 013023 (2015).
[28] M. Mohaghar, J. Carter, B. Musci, D. Reilly, J. McFarland, and D. Ranjan, Evaluation of turbulent mixing transition in a shock-driven variable-density flow, J. Fluid Mech. **831**, 779 (2017).
[29] R. Samtaney, Suppression of the Richtmyer-Meshkov instability in the presence of a magnetic field, Phys. Fluids **15**, L53 (2003).
[30] V. Wheatley, D. I. Pullin, and R. Samtaney, Stability of an Impulsively Accelerated Density Interface in Magnetohydrodynamics, Phys. Rev. Lett. **95**, 125002 (2005).
[31] V. Wheatley, R. Samtaney, and D. Pullin, The Richtmyer-Meshkov instability in magnetohydrodynamics, Phys. Fluids **21**, 082102 (2009).
[32] V. Wheatley, R. Samtaney, D. Pullin, and R. Gehre, The transverse field Richtmyer-Meshkov instability in magnetohydrodynamics, Phys. Fluids **26**, 016102 (2014).
[33] W. Mostert, V. Wheatley, R. Samtaney, and D. I. Pullin, Effects of seed magnetic fields on magnetohydrodynamic implosion structure and dynamics, Phys. Fluids **26**, 126102 (2014).
[34] W. Mostert, V. Wheatley, R. Samtaney, and D. Pullin, Effects of magnetic fields on magnetohydrodynamic cylindrical and spherical Richtmyer-Meshkov instability, Phys. Fluids **27**, 104102 (2015).
[35] A. Miles, D. Braun, M. Edwards, H. Robey, R. Drake, and D. Leibrandt, Numerical simulation of supernova-relevant laser-driven hydro experiments on omega, Phys. Plasmas **11**, 3631 (2004).
[36] A. Miles, B. Blue, M. Edwards, J. Greenough, J. Hansen, H. Robey, R. Drake, C. Kuranz, and D. Leibrandt, Transition to turbulence and effect of initial conditions on three-dimensional compressible mixing in planar blast-wave-driven systems, Phys. Plasmas **12**, 056317 (2005).
[37] F. Grinstein, A. Gowardhan, and A. Wachtor, Simulations of Richtmyer-Meshkov instabilities in planar shock-tube experiments, Phys. Fluids **23**, 034106 (2011).
[38] A. Rasmus, C. Di Stefano, K. Flippo, F. Doss, J. Kline, J. Hager, E. Merritt, T. Desjardins, W. Wan, T. Cardenas *et al.*, Shock-driven discrete vortex evolution on a high-Atwood number oblique interface, Phys. Plasmas **25**, 032119 (2018).
[39] N. Attal and P. Ramaprabhu, Numerical investigation of a single-mode chemically reacting Richtmyer-Meshkov instability, Shock Waves **25**, 307 (2015).
[40] J. A. McFarland, J. A. Greenough, and D. Ranjan, Simulations and analysis of the reshocked inclined interface Richtmyer-Meshkov instability for linear and nonlinear interface perturbations, J. Fluids Engin. **136**, 071203 (2014).
[41] M. Latini, O. Schilling, and W. S. Don, High-resolution simulations and modeling of reshocked single-mode Richtmyer-Meshkov instability: Comparison to experimental data and to amplitude growth model predictions, Phys. Fluids **19**, 024104 (2007).
[42] B. J. Olson and J. A. Greenough, Comparison of two- and three-dimensional simulations of miscible Richtmyer-Meshkov instability with multimode initial conditions, Phys. Fluids **26**, 101702 (2014).
[43] M. T. Henry de Frahan, P. Movahed, and E. Johnsen, Numerical simulations of a shock interacting with successive interfaces using the discontinuous Galerkin method: The multilayered Richtmyer-Meshkov and Rayleigh-Taylor instabilities, Shock Waves **25**, 329 (2015).
[44] W. J. Black, N. A. Denissen, and J. A. McFarland, Evaporation effects in shock-driven multiphase instabilities, J. Fluids Eng. **139**, 071204 (2017).
[45] W. J. Black, N. Denissen, and J. A. McFarland, Particle force model effects in a shock-driven multiphase instability, Shock Waves, 1 (2018).
[46] F. F. Chen, Introduction to plasma physics and controlled fusion, *Plasma Phys.*, Vol. 1 (Plenum press, New York, 1984).
[47] J. B. Middlebrooks, C. Avgoustopoulos, W. J. Black, R. C. Allen, and J. McFarland, Droplet and multiphase effects in a shock-driven hydrodynamic instability with reshock experiments in fluids, Exp. Fluids **20**, 10 (2018).

[48] D. E. Burton, Connectivity structures and differencing techniques for staggered-grid free-lagrange hydrodynamics, Lawrence Livermore National Laboratory, Report No. UCRL-JC-110555, 1992 (unpublished).
[49] D. E. Burton, Consistent finite-volume discretization of hydrodynamic conservation laws for unstructured grids, Lawrence Livermore National Laboratory, Report No. UCRL-JC-118788, 1994 (unpublished).
[50] J. P. Boris and D. L. Book, Flux-corrected transport. I. Shasta, a fluid transport algorithm that works, J. Comput. Phys. **11**, 38 (1973).
[51] J. Fung, A. K. Harrison, S. Chitanvis, and J. Margulies, Ejecta source and transport modeling in the flag hydrocode, Comput. Fluids **83**, 177 (2013).
[52] A. Harrison and J. Fung, Ejecta in the flag hydrocode, Numerical Methods for Multi-Material Fluids and Structures, Pavia, 2009 (unpublished).
[53] S. T. Zalesak, Fully multidimensional flux-corrected transport algorithms for fluids, J. Comput. Phys. **31**, 335 (1979).
[54] T. Barth and D. Jespersen, The design and application of upwind schemes on unstructured meshes, in *27th Aerospace Sciences Meeting* (1989), p. 366.
[55] D. L. Youngs, Time-dependent multi-material flow with large fluid distortion, Numer. Methods Fluid Dyn. **24**, 273 (1982).
[56] V. Wheatley, D. Pullin, and R. Samtaney, Regular shock refraction at an oblique planar density interface in magnetohydrodynamics, J. Fluid Mech. **522**, 179 (2005).
[57] B. Morgan, B. Olson, J. White, and J. McFarland, Self-similarity of a Rayleigh-Taylor mixing layer at low Atwood number with a multimode initial perturbation, J. Turbulence **18**, 973 (2017).
[58] B. J. Olson and J. Greenough, Large eddy simulation requirements for the Richtmyer-Meshkov instability, Phys. Fluids **26**, 044103 (2014).
[59] B. Morgan and J. Greenough, Large-eddy and unsteady RANS simulations of a shock-accelerated heavy gas cylinder, Shock Waves **26**, 355 (2016).
[60] S. K. Shankar, S. Kawai, and S. K. Lele, Two-dimensional viscous flow simulation of a shock accelerated heavy gas cylinder, Phys. Fluids **23**, 024102 (2011).
[61] V. G. Weirs, T. Dupont, and T. Plewa, Three-dimensional effects in shock-cylinder interactions, Phys. Fluids **20**, 044102 (2008).